Feasibility study of a surface-borehole NMR method

Anatoly Legchenko, Benoît Texier, Jean-François Girard, Jean-Michel
Vouillamoz, Fabrice Messan Amene Lawson, Iboukoun Christian Alle,
Jean-Michel Baltassat, Ghislain Pierrat, Marie Boucher

HAL Id: hal-02913683

https://brgm.hal.science/hal-02913683

Submitted on 22 Aug 2022

1   **Feasibility study of a surface-borehole NMR method**

2   by

3   Anatoly Legchenko[1], Benoît Texier[2], Jean-François Girard[3], Jean-Michel Vouillamoz[1],

4   Fabrice Messan Amene Lawson[4], Iboukoun Christian Alle[4], Jean-Michel Baltassat[5], Ghislain

5   Pierrat[2] and Marie Boucher[1]

6

7

8   1. Univ. Grenoble Alps, Institute of Research for Development, IGE, France

9   2. IRIS Instruments, Orléans, France

10   3. IPGS/EOST, Strasbourg University, France

11   4. University of Abomey-Calavi, Bénin

12   5. BRGM, Orléans, France

13

14   **Abstract**

15   We present results of a feasibility study of a borehole induction-coil sensor for surface-

16   borehole NMR (nuclear magnetic resonance - SBNMR) investigations. This sensor of 7 cm

17   diameter and 180 cm length is connected to a standard MRS (Magnetic Resonance Sounding)

18   instrument. Thus, SBNMR is a cost-effective extension of the MRS method. Using a

19   downhole sensor increases the depth of investigation and the resolution of MRS. In the near-

20   horizontal Earth's magnetic field, the sensitive area of the sensor is represented by a cylinder

21   of a few meters in diameter. A blind zone of 0.5 to 1 m around the borehole is due to the

22   disturbance of the Earth's magnetic field by the magnetic core of the sensor. The relatively

23   large volume investigated with SBNMR and the blind zone around borehole may represent an

24   advantage of SBNMR over the NMR borehole tool investigating a narrow zone around the

25   borehole. However, using the Earth's magnetic field renders the SBNMR performance site

26   dependent with an inherently low signal-to-noise ratio. Our first results show a good

27   correspondence between SBNMR, MRS and borehole data.

28

29   *Key words*: MRS, SNMR, surface-borehole, water content, SBNMR

30

Introduction

31

32 Selective sensitivity to groundwater is a major advantage of geophysical methods based on

33 the phenomenon of nuclear magnetic resonance (NMR) compared to other geophysical

34 techniques. NMR-based methods can be applied in a borehole or from surface. Downhole,

35 NMR is mainly used in petroleum exploration and production (Dunn et al., 2002); as these

36 tools were initially developed for deep large-diameter boreholes, they are rarely applied to

37 groundwater investigations. However, recent advances in NMR have allowed developing

38 NMR tools adapted to the small-diameter boreholes typical of hydrogeology (Walsh et al.,

39 2013).

40 Surface NMR (SNMR), also known as Magnetic Resonance Sounding (MRS), is a non-

41 invasive geophysical method (Legchenko and Valla, 2002; Hertrich, 2008; Legchenko, 2013;

42 Behroozmand et al., 2015). MRS and borehole NMR are based on the same physical

43 phenomenon and have many common features, but these methods are not interchangeable

44 (e.g. Müller-Petke et al., 2011). The maximum depth of investigation with MRS is site

45 dependent and rarely exceeds 100 m (Legchenko et al., 1997). The resolution is also variable

46 and progressively decreases with increasing depth (e.g. Girard et al., 2007; Müller-Petke and

47 Yaramanci, 2008; Hertrich et al., 2009; Chevalier et al, 2014; Parsekian and Grombacher,

48 2015). A limited investigation depth and relatively poor resolution are the properties of MRS

49 (Legchenko and Pierrat, 2014).

50 Stoeffl (2001) proposed to improve MRS by combining surface and borehole NMR

51 methods. Using a transmitting loop on the surface and a magnetic-field sensor downhole, we

52 obtain surface-borehole NMR (SBNMR). The possibility of using with MRS a small

53 magnetic-field sensor instead of a large loop was demonstrated by Davis et al. (2014) using a

54 SQUID sensor. However, the use of a SQUID sensor for SBNMR is not absolutely necessary

55 and we developed a more traditional induction-coil sensor. Hereafter, we report the first

56 experimental results.

Surface-borehole NMR

57

58 Practical implementation of the SBNMR method can be done with a standard MRS

59 instrument equipped with an additional induction-coil sensor in the borehole. Figure 1 shows

60 the measuring setup consisting of a transmitting loop (Tx) on the surface and a sensor in the

61 borehole (Rx).
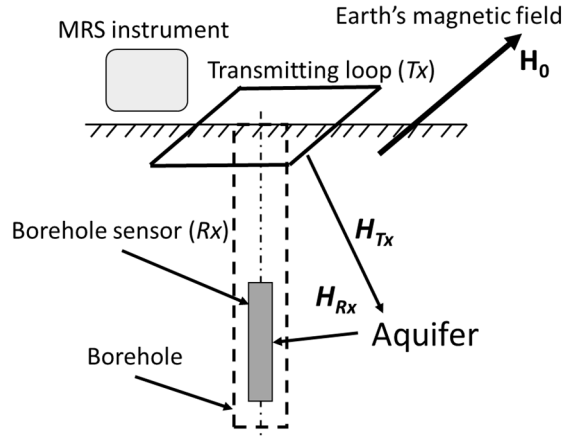
Fig. 1. Transmitting loop on the surface (Tx) and the induction-coil sensor downhole (Rx)

For measuring, a pulse of alternative current oscillating with the Larmor frequency is generated in the transmitting loop, producing the excitation magnetic field H_{Tx}. The pulse is characterized by a pulse moment being a product of the current amplitude and duration After the pulse is terminated, groundwater generates a magnetic field H_{Rx}, which induces a voltage in the induction coil in the borehole. Both, sensor position and current magnitude in the loop can be varied. Records of the magnetic resonance signal at each combination of sensor depth and pulse moment provide data for interpretation.

Sensor design

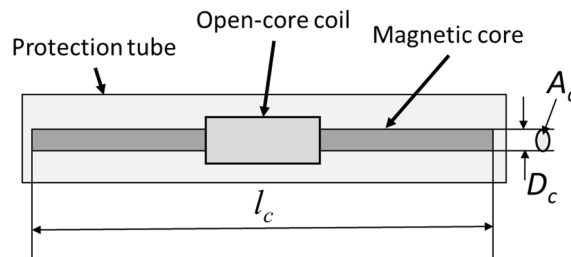Our sensor consists of an open-core coil with a ferrite core (Fig. 2). The coil and connecting cables are protected by electrostatic screens. The sensor is mechanically protected by a plastic tube.

Fig. 2. Design of the borehole sensor (l_c – length of the core, D_c – diameter of the core, A_c – area of the core)

The voltage induced in a coil is given by Faraday's law:

$$V = -\mu_0 \mu_c n A_c \frac{dH}{dt},$$ (1)

82   where $\mu_0 = 4\pi \times 10^{-7}$ H/m, μ_c is the resultant permeability of the core, n is a number of

83   turns in the coil and A_c is the core cross-section area. The resultant permeability μ_c may be

84   smaller than the core material permeability μ_r due to the demagnetizing field effect:

85
$$\mu_c = \frac{\mu_r}{1 + N_d(\mu_r - 1)}, \qquad (2)$$

86   where N_d is demagnetizing factor that is dependent on the core geometry. It can be estimated

87   as (Tumanski, 2007):

88
$$N_d \cong \frac{D_c^2}{l_c^2}\Big(\ln(2l_c / D_c) - 1\Big), \qquad (3)$$

89   where D_c and l_c are the diameter and length of the core, respectively.

90   Thus, the transfer function between the magnetic field and the voltage induced in the coil

91   depends on the effective area $A_{eff} = n\mu_c A_c$ defined by the magnetic permeability of the

92   material and the sensor geometry. For estimating the sensor parameters, we considered a

93   ferrite core with $\mu_r = 2300$ and used Eqs. 1-3. Fig. 3a shows the resultant magnetic

94   permeability μ_c *versus* core diameter and, considering different core lengths, shows that if

95   the l_c / D_c ratio increases then $\mu_c \rightarrow \mu_r$. Fig. 3b shows the effective area *versus* the core

96   diameter, and Fig. 3c demonstrates that for a fixed core length the effective area cannot be

97   significantly increased by increasing μ_r.
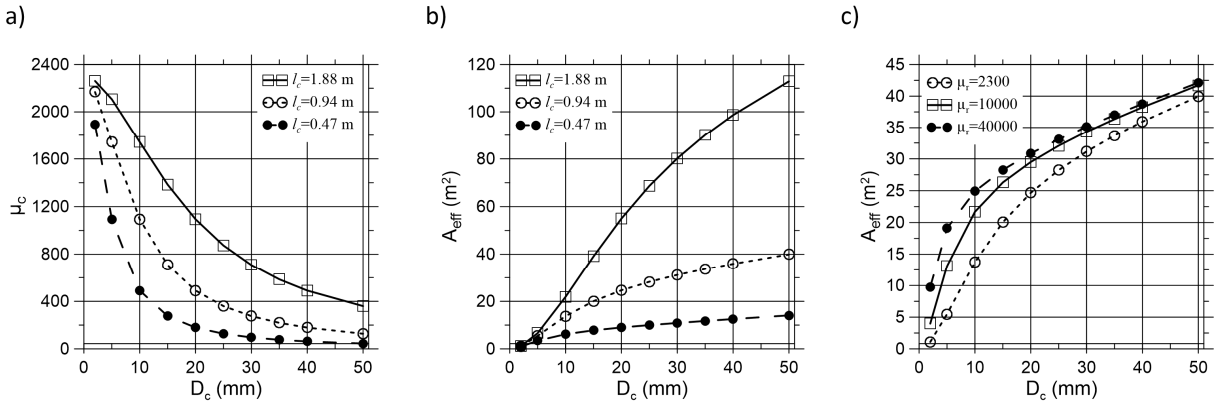
Fig. 3a) The resultant magnetic permeability of the core versus core diameter computed considering different core lengths (μ_r=2300). b) The effective area versus core diameter (μ_r=2300). c) The effective area computed considering different magnetic-permeability values of the material and fixed core length (l_c=0.94 m).

Fig. 3 suggests using a long core of large diameter, but sensor dimensions are limited by practical considerations such as the borehole diameter as well as the facility of shipping and handling. To start with, we fabricated a sensor with an external diameter of 70 mm. The core (l_c=1767 mm) was made of ferrite bars with dimensions of 27.5×30×93 mm^3 and $\mu_r = 2300 \pm 20\%$ (1840 - 2760) at 25 °C. The ferrite bar geometry is guaranteed by the manufacturer with an accuracy of ±2%. Our coil contains 160 turns and has a resistivity of 1.35 Ω; Eqs. 1 to 3 allow computing $A_{eff} = 78.7$ m^2. For modelling, we can represent the sensor by a magnetic dipole with the respective surface area.

Between 0 °C and 30 °C the ferrite magnetic permeability has an almost linear temperature dependence, changing with a temperature coefficient of 0.7%/°. At 0 °C $\mu_r = 1900$ and at 30 °C it is $\mu_r = 2380$. The corresponding effective area changes from 74.7 m^2 to 79.4 m^2 (from -5% to 0.9%) with a consequent impact on the measured voltage. The uncertainty in the magnetic permeability of ferrite causes a corresponding uncertainty in the effective area from 73.9 m^2 to 82.3 m^2 (from -4.5% to 6%). Thus, without calibration, variations in core magnetic permeability can cause an uncertainty in measuring voltage of up to ±6%.

Noise considerations

The accuracy of the signal measurements depends on the noise level. Electromagnetic noise is generated by different sources, such as the amplifier, the coil wire, the magnetic core
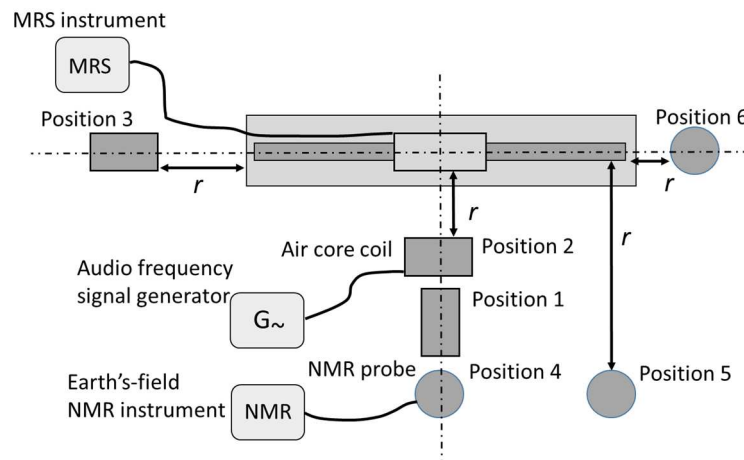
and several other external sources. As the core is not exposed to mechanical or magnetic stress, we exclude a noise due to the Backhausen effect as well as other possible noises generated by the ferrite core. The coil wire produces thermal noise that can be estimated as:

$$V_T = 2\sqrt{k_B T \, \Delta f \, R} , \qquad (4)$$

where $k_B = 1.38 \times 10^{-23}$ J/K is the Boltzmann constant, T is the temperature, Δf is the bandwidth and R is the wire resistance.

Considering a bandwidth of $\Delta f = 300$ Hz (NUMIS[poly] MRS instrument), $T = 293$ °K and wire resistance $R = 1.35$ Ω, we obtain a thermal noise of 2.6 nV (0.15 nV/Hz$^{-1/2}$). This noise can be reduced by lowering the wire resistivity. Amplifier noise reported by MRS instrument manufacturers varies between 0.1 and 1.78 nV/Hz$^{-1/2}$, yielding a noise voltage varying between 1.7 and 31 nV ($\Delta f = 300$ Hz). In practice, external noise is added to amplifier noise. When using a large loop, the external noise is much larger than the amplifier noise. For example, during our MRS study on the Greenland ice sheet, far from everything (Legchenko et al., 2018), the natural external noise measured with a typical MRS loop (80×80 m^2) slightly varied around 100 nV. Such noise may be several times larger during magnetic storms. In built-up areas, manmade noise can be much larger than atmospheric one. However, when using borehole sensors as well as small receiving loops (Grombacher et al., 2018), external noise voltage may be equal to or even smaller than the amplifier noise, and the amplifier design becomes an important issue.

*S*he borehole sensor in laboratory, for which we used an experimental setup shown in Fig. 4.

*Fig. 4. The experimental setup for measuring parameters of the induction-coil sensor*

146   An Earth's-field NMR instrument with a water sample probe (Clément et al., 2011)

147   evaluated the heterogeneity of the Earth's magnetic field disturbed by the sensor core. Fig. 5

148   shows the relaxation time T_2^* and the Larmor frequency both characterizing the homogeneity

149   of the Earth's magnetic field. Far from the sensor, the relaxation time was T_2^*=585 ms, the

150   Larmor frequency being 1969 Hz. Then, the probe with the water sample was placed at

151   different distances from the sensor (positions 4 to 6), and we measured the Larmor frequency

152   and the relaxation time T_2^* again. At less than 50 cm, the free-induction decay signal (FID)

153   could not be measured because of short T_2^* values; only spin-echo (SE) measurements

154   allowed observing the NMR signal in the vicinity of the sensor. At larger distances, the FID

155   signal was well observed. Our results show that at about 0.5 to 1 m around the sensor the FID

156   signal is well measured, but the relaxation time is shortened and the Larmor frequency is

157   shifted. At 1 to 2 m from the sensor, the measurements are moderately disturbed and beyond

158   2 m the Earth's magnetic field is only slightly disturbed.
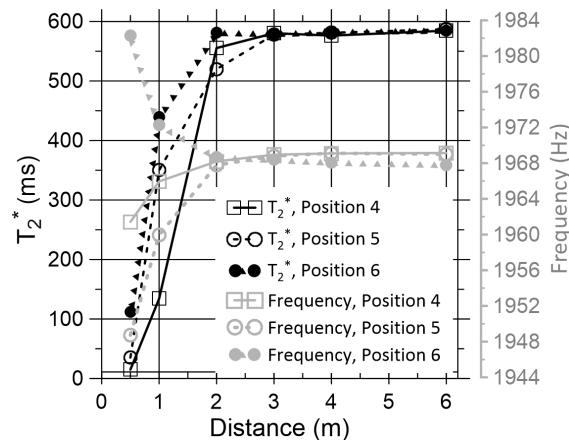
159

160   *Fig. 5. Relaxation time T_2^* (left vertical axis) and Larmor frequency (right vertical axis)*

161   versus *distance between sensor and water sample.*

162

163   Then, the sensor was connected to the MRS instrument. To estimate the max radial extent

164   of the sensitive volume, an audio-frequency generator connected to an air core coil was used

165   for generating a test signal and the MRS instrument applied as a simple voltmeter measured

166   voltage induced in the sensor coil. Both, generator and MRS instrument were tuned to the

167   same frequency of 1969 Hz. We set the coil at different positions around the sensor (positions

168   1-3) and measured voltage *versus* distance r between coil and sensor. The normalized

169   amplitude of the signal *versus* distance is shown on Fig. 6.
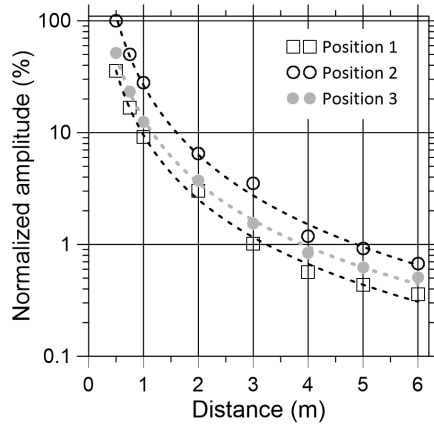
Fig. 6. Normalized amplitude of the test signal measured at different positions of the transmitting coil versus *distance between sensor and coil. Dashed lines show the power fit of experimental data.*

These measurements show that voltage induced by the test coil rapidly decreased with distance and 6 m from the sensor the amplitude represented only about 0.6% of the initial value measured at 0.5 m. For each position, the measured amplitudes were fitted by a function $e = a_i / r^b$ (dashed lines). For positions 1 and 3, $b = 1.9$ and for position 2, $b = 2.1$. The fitting coefficient a_i has individual values for each position. These measurements showed that near the real sensor, the sensitivity decreases with a rate of approximately $\sim 1/r^2$.

Fig. 6 shows the sensitivity of the sensor to a local signal source (air-core coil). However, the NMR signal is produced by a volume of water around the borehole, which increases as a square function of distance; therefore, the sensitive zone of the sensor can be extended beyond the estimate shown on Fig. 6. However, the volume of water that produces an NMR signal is dependent upon the excitation magnetic field generated by the transmitting loop as well as upon the inclination of the Earth's magnetic field; these parameters are site dependent and required more detailed investigations, which was outside the scope of this study.

Forward modelling

For measuring a magnetic resonance signal from groundwater, an alternating-current pulse with amplitude I_0 and duration τ was generated in the transmitting loop on surface. After switching off the current, the subsurface water generates an exponentially decaying magnetic

192   field that oscillates with the Larmor frequency ω_0. The voltage induced in the measuring coil

193   can be calculated as (Weichman et al., 2000; Hertrich et al., 2005):

$$V(q,t) = \int K(\mathbf{r},q) \int w(\mathbf{r},T_2^*) \exp(-t/T_2^*) dT_2^* d\mathbf{r} \ , \qquad (5)$$

195   where $q = I_0 \tau$ is the pulse moment, $w(\mathbf{r},T_2^*)$ is distribution water in the subsurface and

196    $K(\mathbf{r},q)$ is the kernel function describing spatial sensitivity. If investigating only the water

197   content, then the initial amplitude of the magnetic-resonance signal is sufficient, and the

198   relaxation term can be omitted. Compared to the MRS method, the depth of the sensor in the

199   borehole introduces an additional parameter that allows improving vertical resolution, and the

200   kernel must be calculated considering each position of the sensor.

201   **Inverse modelling**

202   The MRS inverse problem can be considered as linear, and we approximate the integral

203   equation of Eq. 5 by the matrix equation

$$\mathbf{A}\mathbf{w} = \mathbf{v}, \qquad (6)$$

205   where $\mathbf{v} = v_1, v_2, ..., v_i, ..., v_I$ is a set of experimental data, $\mathbf{w} = w_1, w_2, ..w_j, ..., w_J$ is the solution

206   vector and $\mathbf{A}$ is a $I \times J$ matrix representing the kernel of Eq. 5.

207   We assumed a horizontal stratification (1-D inverse problem) and represented the

208   subsurface by J homogeneous layers. Elements of the solution vector (w_j) represented the

209   water content in corresponding layers. Elements of the data vector v_i included the voltage

210   measured in the receiving coil at each sensor position *versus* pulse moment in the transmitting

211   loop. The total number of measured points $I = \sum_{m=1}^{M} N_m$, where M is the number of sensor

212   positions and N_m is the number of pulse moments, corresponding to position m. The matrix

213    $\mathbf{A}$ is built in accordance with the measuring procedure.

214   During our study, we set the sensor at one depth and made measurements for all pulse

215   moments. Then, we changed the depth and repeated the measurements. Note that, compared

216   to MRS, the measurements at each sensor position required fewer pulse moments. One may

217   use only pulse moments corresponding to the maximum sensitivity around the sensor

218 position. Each element $a_{i,j}$ of matrix **A** was computed with Eq. 5 and contained the

219 amplitude of the magnetic resonance signal corresponding to sensor depth and the value of

220 pulse moment (Fig. 7).
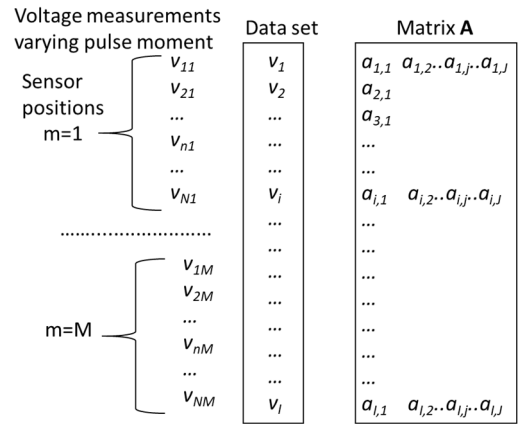
221

222 *Fig. 7. SBNMR data prepared for inversion.*

223

224 We used the time-step inversion (Legchenko et al., 2002) based on the Tikhonov

225 regularization method. Other existing algorithms, such as the QT inversion (Mueller-Petke

226 and Yaramanci, 2010), are applicable as well.

227 **Field measurements**

228 For testing the SBNMR method, we performed measurements in the southern part of the

229 Republic of Benin. The township of Abomey Calavi is located between the latitudes

230 6°20'23.4" and 6°42'6.6" North, and the longitudes 2°14'13.8" and 2°25'7.8" East. At the

231 Ouédo test site, the Tertiary "Continental Terminal" formation is rather irregular, but makes

232 up a good aquifer (Hounsinou et al., 2014). It is composed of intercalations of fine to coarse

233 sand layers with clay patterns (Lang et al., 1990) shown in Figs. 8a and 8b.

234
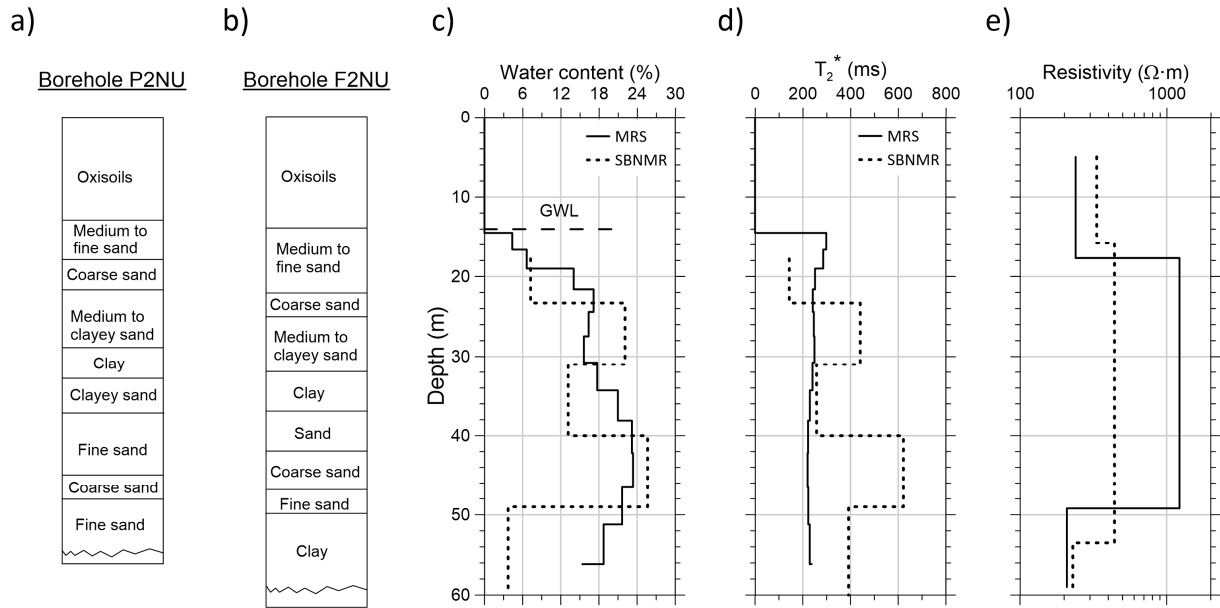
Fig. 8. a,b) Lithological logs of boreholes P2NU and F2NU used for SBNMR experiments. c) Water content distribution provided by MRS sounding (solid line) and by SBNMR measurements (dashed line). d) Corresponding relaxation time T_2^*. e) Electrical resistivity of the subsurface derived from TEM measurements (two equivalent models).

The substratum of this aquifer is composed of continuous clay. The average depth of the substratum, as identified by 15 electrical soundings (VES), is 112 m (90 to 140 m) with an average resistivity of 64 Ω·m (between 200 and 30 Ω·m). The aquifer formation has an average resistivity of 380 Ω·m (between 750 and 90 Ω·m). Because of the relatively high electrical resistivity and small thickness, the clay layers within the aquifer formation were not resolved by 15 VES and 31 transient EM (TEM) soundings. The average borehole depth is 143 m (110 to 171 m).

In the study area, the inclination of the Earth's magnetic field is 5°N and the Larmor frequency is about 1393 Hz. For our study, we used a commercially available NUMIS[poly] MRS instrument (Iris Instruments). The induction-coil sensor was placed in borehole F2NU (PVC casing) and the transmitting loop (25-m-side square, 3 turns) was laid out around it. Another borehole (P2NU) was located 10 m from F2NU. An MRS sounding with a coincident figure-eight square loop (62.5-m-side) was set up around borehole F2NU. The length of the cable connecting the instrument and the sensor was 50 m, which defined the deepest position of the sensor. The amplitude of the NMR signal measured with the downhole sensor is a function of both pulse moment and sensor depth. It has a typical for MRS a half-sinus-wave shape. We selected values of the pulse moment individually for each depth so that we always

258   observed a maximum SBNMR signal. To improve the signal to noise ratio (SNR), we used

259   stacking (usually close to 100). Logging data were not available for these boreholes and we

260   additionally carried out Transient EM (TEM) measurements using a TemFast-48 instrument

261   (AERM) with a coincident 100-m-side square loop. For interpreting the MRS measurements,

262   we used Samovar software (IRD) and for TEM data IX1D v.3.6 (Interpex). The SBNMR data

263   set was processed with experimental software developed by the authors. Figs. 8a and 8b show

264   the lithological logs of two boreholes, ten metres in-between and both located within the

265   transmitting loop. The core analysis shows that both boreholes intersected sand and clay

266   layers, but not at the same levels, demonstrating the lateral heterogeneity of the subsurface.

267   This heterogeneity was neither resolved by MRS sounding (Figs. 8c and 8d) nor by TEM

268   sounding (Fig. 8e). For the MRS and TEM measurements we used large loops and signals

269   from heterogeneous formations were thus averaged. SBNMR shows differences in water

270   content between three zones, but the resolution was insufficient for clearly distinguishing in-

271   between. The sensor was in borehole F2NU and both, high values of the water content (22

272   and 25%) and long relaxation time (440 and 622 ms) suggest two coarse sand layers (23-31 m

273   and 40-49 m). These layers are separated by a less permeable layer with the average water

274   content of 13% and the relaxation time of 258 ms (31-40 m), identified as clay and sand

275   formations. The correspondence between SBNMR and borehole results is not perfect, which

276   may be explained by the scale factor affecting both data sets. The lithological logs show

277   results corresponding to the layers intersected by the borehole and SBNMR provides

278   information averaged over the volume defined by sensor sensitivity.

279   Here, we present the SBNMR measurements with the sensor set at six different depths

280   from 22 to 49.5 m. Before stacking and filtering, the noise varied between 20 and 30 nV.

281   Fig. 9 shows the entire SBNMR data set used for inversion. For each position of the

282   downhole sensor, time series are recorded with a few different values of the pulse moment.

283   Each record consists of measuring ambient EM noise before the pulse and SBNMR signal

284   after the pulse. The dead time between the end of the pulse and the signal recording was 40

285   ms. Fig. 9a shows time records plotted versus time (0-192 ms) and sensor positions (0-5). The

286   right vertical axis (grey colour) shows the correspondence between the sensor position and the

287   depth of the top of the sensor. For each sensor position, time series are plotted considering

288   normalized pulse moments. For example, a record plotted at the sensor position 0 corresponds

289   to the minimum pulse moment, and the maximum pulse moment corresponds to the positon 1

290   (left vertical axis). Corresponding ambient EM noise records are shown in Fig. 9c. Fig 9b

291   shows theoretical SBNMR signals computed after the inverse model; and Fig. 9d shows the

misfit between measured and theoretical signals. The misfit was computed as the root mean square error between experimental and theoretical time series.
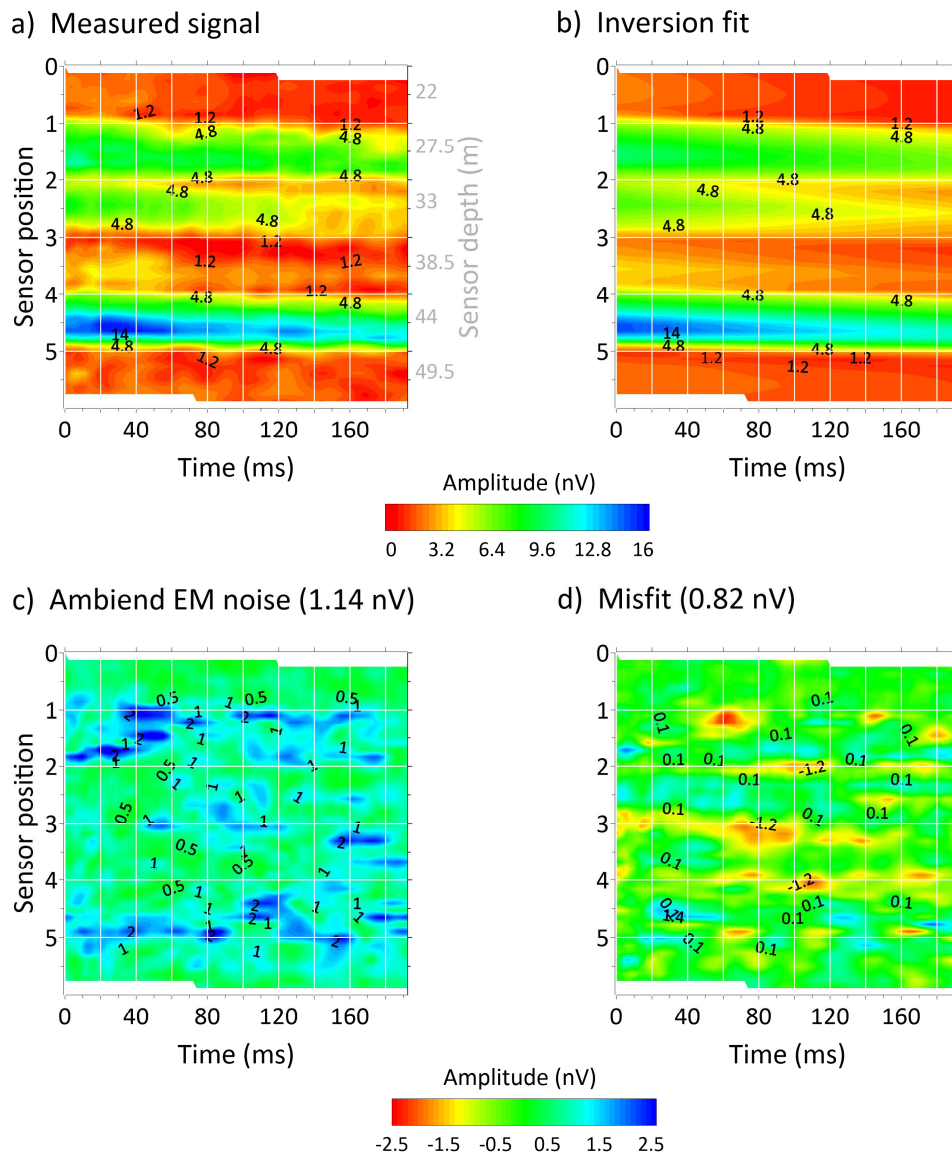
Fig. 9. a) Amplitude of SBNMR signal (colour scale) versus *time (after the dead time) recorded at different sensor positions (left vertical scale). For each sensor position, the right vertical axis (grey colour) shows a depth corresponding to the sensor top. b) Theoretical signal computed after the inverse model. c) Noise records corresponding to the same time series. d) The misfit between measured and theoretical signals.*

Fig. 10 shows time records extracted from the data shown in the previous figure. Each graph corresponds to one of the sensor positions. Solid lines show the envelope of the signal amplitude *versus* time and the dashed lines show the noise amplitude recorded before the

305 pulse. At all sensor positions, the SBNMR signal clearly dominates noise, thus confirming the

306 feasibility of our SBNMR measurements. These examples also demonstrate pronounced

307 differences between SBNMR signals recorded at different depths corresponding to different

308 geological patterns. Theoretical signals computed after the inverse models fit measured data

309 with the error of 0.82 nV and the mean noise was 1.14 nV.
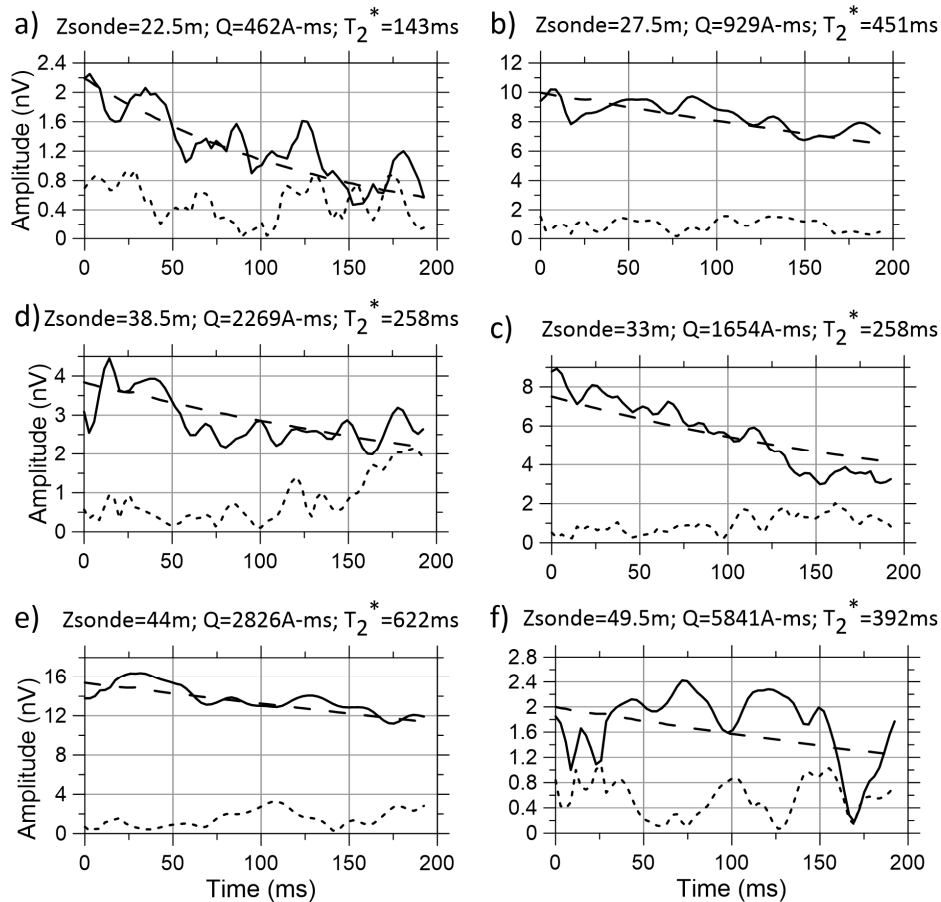
310

311 *Fig. 10. SBNMR records measured with the sensor located at different depths. Solid lines*

312 *show the SBNMR signal recorded after the dead time following the pulse, long-dashed lines*

313 *show inversion fits and short-dashed lines show noise records before the pulse.*

314

315 **Discussion**

316 Our experimental study has confirmed the feasibility of surface-borehole NMR

317 measurements. SBNMR is both similar and different compared to both MRS and borehole

318 NMR, but provides information about groundwater unavailable with the last two methods.

319   Borehole NMR uses an artificial static magnetic field that allows a high sensitivity. The

320 depth resolution of borehole NMR and the maximum depth of investigation are also much

321 better than with SBNMR and MRS. However, borehole NMR investigates only a narrow zone

322 around borehole, the sensitive area being located within the walls of a cylinder. The diameter

of this (virtual) cylinder (<40 cm) and the wall thickness (<2 mm) are determined by the gradient of the static magnetic field (Dunn et al., 2002). Consequently, hydraulic parameters of the aquifer formation investigated with borehole NMR should be considered as local data. Additionally, some zone around the borehole can be modified by drilling, affecting the results of the study. On the contrary, MRS and SBNMR provide data averaged over large undisturbed volumes.

Operating in the geomagnetic field, MRS and SBNMR both have low sensitivity and a poor signal-to-noise ratio. Results are averaged over a large investigated area that depends on the size of the transmitting loop. SBNMR has better vertical resolution and a potentially larger depth of investigation than MRS. It also better characterizes the investigated aquifer formations in terms of geometry, porosity and hydraulic conductivity. Measurements of both T_1 and T_2 are available with SBNMR as well as with MRS (Legchenko et al., 2004; 2010).

As we have shown the feasibility of this type of measurements, we think that our principal goal was achieved.

Conclusions

We developed and successfully tested in a near-horizontal Earth's magnetic field a borehole sensor for surface-borehole NMR investigations. SBNMR results are averaged over the sensitive area of the sensor that spreads out to a few meters around the borehole. Groundwater at up to 1 m around borehole does not produce a measurable SBNMR signal because of the strong disturbance of the Earth's magnetic field by the magnetic core of the sensor. Similar to MRS, the performance of SBNMR is site dependent and the inherently poor signal-to-noise ratio is comparable to that of MRS.

Acknowledgements

355   The content of this paper is the responsibility of the authors and cannot be regarded as

356   reflecting the position of the European Union or the African Union.

357   **References**

358   Behroozmand, A.A., Keating, K., Auken, E., 2015. A review of the principles and

359   applications of the NMR technique for near-surface characterization. Surv. Geophys.,

360   36(1), 27-85, doi: 10.1007/s10712-014-9304-0.

361   Chevalier, A., Legchenko, A., Girard, J.F., Descloitres, M., 2014. 3D Monte Carlo inversion

362   of magnetic resonance measurements. Geophys. J. Intern., 198(1), 216-228, doi:

363   10.1093/gji/ggu091.

364   Clément, R., Legchenko, A., Quetu, M., Descloitres, M., Oxarango, L., Guyard H., Girard,

365   J.F., 2011. Experimental study of a domestic waste material using magnetic resonance

366   measurements. Near Surf. Geophys., 9, 179-185, doi: 10.3997/1873-0604.2010069.

367   Davis, A.C., Dlugosch, R., Queitsch, M., Macnae, J.C., Stolz, R., Müller-Petke, M., 2014.

368   First evidence of detecting surface nuclear magnetic resonance signals using a compact B-

369   field sensor, Geophys. Res. Lett., 41, 4222–4229, doi:10.1002/2014GL060150.

370   Dunn, K.J., Bergman, D.J., Latorraca, G.A., 2002. Nuclear Magnetic Resonance

371   Petrophysical and Logging Applications. Elsevier Science Ltd, UK.

372   Girard, J-F, Boucher, M., Legchenko, A., Baltassat, J.M., 2007. 2D magnetic resonance

373   tomography applied to karstic conduit imaging. J. Appl. Geophys., 63, 103-116, doi:

374   10.16/j.jappgeo.2007.08.0001.

375   Grombacher, D., Liu, L., Larsen, J.J., Auken, E., 2018. Practical considerations for small

376   receive coils in surface NMR. J. Appl. Geophys., 154, 81-92, doi:

377   10.1016/j.jappgeo.2018.04.005.

378   Hertrich, M., Braun, M., Yaramanci, U., 2005. Magnetic resonance soundings with separated

379   transmitter and receiver loops. Near Surf. Geophys., 3(3), 131–144, doi:10.3997/1873-

380   0604.2005010.

381   Hertrich, M., 2008. Imaging of groundwater with nuclear magnetic resonance. Prog. Nucl.

382   Magn. Reson. Spectrosc., 53(4), 227–248, doi:10.1016/j.pnmrs.2008.01.002.

383   Hertrich, M., Green, A.G., Braun, M., Yaramanci, U., 2009. High-resolution surface-NMR

384   tomography of shallow aquifers based on multi-offset measurements. Geophysics, 74,

385   G47-G59, doi:10.1190/1.3258342.

386   Hounsinou, P., Mama, D., Alassane, A., Boukari, M., 2014. Hydrogeology and Chemistry

387   Synthesis of the deep Boring of the Township of Abomey-Calavi, Benin. Res. J. Chem.

388   Sci., 4(12), 98-102.

389   Lang, J., Kogbe, C., Alidou, S., Alzouma, K.A., Bellion, G., Dubois, D., Durand, A., Guiraud,

390   R., Houessou, A., de Klasz, I., Romann, E., Salard-Cheboldaeff, M., Trichet, J., 1990. The

391   Continental Terminal in West Africa. J. Afr. Earth Sci., 10(1-2), 79-99, doi: 10.1016/0899-

392   5362(90)90048-J.

393   Legchenko, A.V., Beauce, A., Guillen, A., Valla, P., Bernard, J., 1997. Natural variations in

394   the magnetic resonance signal used in PMR groundwater prospecting from the surface.

395   Eur. J. Environ. Eng. Geophys., 2, 173-190.

396   Legchenko, A., Valla, P., 2002. A review of the basic principles for proton magnetic

397   resonance sounding measurements. J. Appl. Geophys., 50, 3–19., doi: 10.1016/S0926-

398   9851(02)00127-1.

399   Legchenko, A., Baltassat, J.M., Beauce, A., Bernard, J., 2002. Nuclear magnetic resonance as

400   a geophysical tool for hydrogeologists. J. Appl. Geophys., 50, 21-46, doi:10.1016/S0926-

401   9851(02)00128-3

402   Legchenko, A., Baltassat, J.M., Bobachev, A., Martin, C., Robin, H., Vouillamoz, J.M., 2004.

403   Magnetic resonance sounding applied to aquifer characterization. J. Ground Water, 42(3),

404   363–373, doi: 10.1111/j.1745-6584.2004.tb02684.x.

405   Legchenko, A., Vouillamoz, J.M., Roy, J., 2010. Application of the magnetic resonance

406   sounding method to the investigation of aquifers in the presence of magnetic materials.

407   Geophysics, 75(6), L91–L100, doi: 10.1190/1.3494596.

408   Legchenko, A., 2013. Magnetic Resonance Imaging for Groundwater. Wiley-ISTE 978-1-

409   84821-568-9.

410   Legchenko A., Pierrat, G., 2014. Glimpse into the design of MRS instrument. Near Surf.

411   Geophys., 12, 297 – 308, doi:10.3997/1873-0604.2014006.

412   Legchenko, A., Miège, C., Koenig, L.S., Forster, R.R., Miller, O., Solomon, D.K., Schmerr,

413   N., Montgomery, L., Ligtenberg, S., Brucker, L., 2018. Estimating water volume stored in

414   the south-eastern Greenland firn aquifer using Magnetic-Resonance Soundings. J. Appl.

415   Geophys., 150, 11–20, doi: 10.1016/j.jappgeo.2018.01.005.

416   Müller-Petke M., Yaramanci, U., 2008. Resolution studies for Magnetic Resonance Sounding

417   (MRS) using the singular value decomposition. J. Appl. Geophys., 66, 165–175, doi:

418   10.1016/j.jappgeo.2007.11.004.

419   Mueller-Petke, M., Yaramanci, U., 2010. QT inversion — Comprehensive use of the

420   complete surface NMR data set. Geophysics, 75, 4, WA199–WA209, doi:

421   10.1190/1.3471523.

422 Müller-Petke, M., Hiller, T., Herrmann, R., Yaramanci, U., 2011. Reliability and limitations

423   of surface NMR assessed by comparison to borehole NMR. Near Surf. Geophys., 9, 123–

424   34, doi: 10.3997/1873-0604.2010066.

425 Parsekian, A.D., Grombacher, D., 2015. Uncertainty estimates for surface nuclear magnetic

426   resonance water content and relaxation time profiles from bootstrap statistics. J. Appl.

427   Geophys. 119, 61–70, doi: 10.1016/j.jappgeo.2015.05.005.

428 Stoeffl, W., 2001. Use of earth field spin echo NMR to search for liquid minerals. Patent N°

429   US 6,177,794 Bl.

430 Tumanski, S., 2007. Induction coil sensors—a review. Meas. Sci. Technol. 18, R31–R46, doi:

431   10.1088/0957-0233/18/3/R01.

432 Walsh, D., Turner, P., Grunewald, E., Zhang, H., Butler, J.J.Jr., Reboulet, E., Knobbe, S.,

433   Christy, T., Lane, J.W. Jr., Johnson, C.D., Munday, T., Fitzpatrick, A., 2013. A small-

434   diameter NMR logging tool for groundwater investigations. J. Ground Water, 51(6), 914–

435   926, doi:10.1111/gwat.12024.

436 Weichman, P.B., Lavely, E.M., Ritzwoller M.H., 2000. Theory of surface nuclear magnetic

437   resonance with applications to geophysical imaging problems, Phys. Rev. E, 62(1), 1290–

438   1312, doi:10.1103/PhysRevE.62.1290.

439

Figure captions

441   *Fig. 1. Transmitting loop on the surface (Tx) and the induction-coil sensor downhole (Rx)*

442   *Fig. 2. Design of the borehole sensor (l_c – length of the core, D_c – diameter of the core, A_c*

443 *– area of the core)*

444   *Fig. 3a) The resultant magnetic permeability of the core* versus *core diameter computed*

445 *considering different core lengths (μ_r=2300). b) The effective area* versus *core diameter*

446 *(μ_r=2300). c) The effective area computed considering different magnetic-permeability values*

447 *of the material and fixed core length (l_c=0.94 m).*

448   *Fig. 4. The experimental setup for measuring parameters of the induction-coil sensor*

449   *Fig. 5. Relaxation time T_2^* (left vertical axis) and Larmor frequency (right vertical axis)*

450 versus *distance between sensor and water sample.*

451   *Fig. 6. Normalized amplitude of the test signal measured at different positions of the*

452 *transmitting coil* versus *distance between sensor and coil. Dashed lines show the power fit of*

453 *experimental data.*

454   *Fig. 7. SBNMR data prepared for inversion.*

455   *Fig. 8. a,b) Lithological logs of boreholes P2NU and F2NU used for SBNMR experiments.*

456   *c) Water content distribution provided by MRS sounding (solid line) and by SBNMR*

457   *measurements (dashed line). d) Corresponding relaxation time T_2^*. e) Electrical resistivity of*

458   *the subsurface derived from TEM measurements (two equivalent models).*

459   *Fig. 9. a) Amplitude of SBNMR signal (colour scale)* versus *time (after the dead time)*

460   *recorded at different sensor positions (left vertical scale). For each sensor position, the right*

461   *vertical axis (grey colour) shows a depth corresponding to the sensor top. b) Theoretical*

462   *signal computed after the inverse model. c) Noise records corresponding to the same time*

463   *series. d) The misfit between measured and theoretical signals.*

464   *Fig. 10. SBNMR records measured with the sensor located at different depths. Solid lines*

465   *show the SBNMR signal recorded after the dead time following the pulse, long-dashed lines*

466   *show inversion fits and short-dashed lines show noise records before the pulse.*

467